nature photonics

LETTERS

PUBLISHED ONLINE: 11 MAY 2015 | DOI: 10.1038/NPHOTON.2015.69

Inverse design and demonstration of a compact and broadband on-chip wavelength demultiplexer

Alexander Y. Piggott, Jesse Lu, Konstantinos G. Lagoudakis, Jan Petykiewicz, Thomas M. Babinec and Jelena Vučković*

Integrated photonic devices are poised to play a key role in a wide variety of applications, ranging from optical interconnects[1] and sensors[2] to quantum computing[3]. However, only a small library of semi-analytically designed devices is currently known[4]. Here, we demonstrate the use of an inverse design method that explores the full design space of fabricable devices and allows us to design devices with previously unattainable functionality, higher performance and robustness, and smaller footprints than conventional devices[5]. We have designed a silicon wavelength demultiplexer that splits 1,300 nm and 1,550 nm light from an input waveguide into two output waveguides, and fabricated and characterized several devices. The devices display low insertion loss (~2 dB), low crosstalk (<−11 dB) and wide bandwidths (>100 nm). The device footprint is 2.8 × 2.8 μm^2, making this the smallest dielectric wavelength splitter.

Electronic hardware description languages such as Verilog and VHDL are widely used in industry to design digital and analogue circuits[6,7]. The automation of large-scale circuit design has enabled the development of modern integrated circuits that can contain billions of transistors. Photonic devices, however, are effectively designed by hand. The designer selects an overall structure based on analytic theory and intuition, and then fine-tunes the structure using brute-force parameter sweep simulations. Due to the undirected nature of this process, only a few degrees of freedom (two to six) are available to the designer. The field of integrated photonics would be revolutionized if the design of optical devices could be automated to the same extent as circuit design.

We have previously developed an algorithm that can automatically design arbitrary linear optical devices[5]. Our method allows the user to 'design by specification', whereby the user simply specifies the desired functionality of the device, and the algorithm finds a structure that meets these requirements. In particular, our algorithm searches the full design space of fabricable devices with arbitrary topologies. These complex, aperiodic structures can provide previously unattainable functionality, or higher performance and smaller footprints than traditional devices, due to the greatly expanded design space[5,8–14]. Our algorithm uses local-optimization techniques based on convex optimization[15] to efficiently search this enormous parameter space.

Here, we demonstrate the capabilities of our inverse design algorithm by designing and experimentally demonstrating a compact wavelength demultiplexer on a silicon-on-insulator (SOI) platform. One of the key functions of silicon photonics is wavelength division multiplexing (WDM), which multiplies the data capacity of a single optical waveguide or fibre-optic cable by the number of wavelength channels used[16–18]. Unfortunately, conventional wavelength demultiplexers such as arrayed waveguide gratings[19], echelle grating demultiplexers[20] and ring resonator arrays[21] are fairly large, with dimensions ranging from tens to hundreds of micrometres[22]. Our device has a footprint of only $2.8 \times 2.8\ \mu m^2$, which is considerably smaller than any previously demonstrated dielectric wavelength splitter[23].

Let us now consider the general formulation of the inverse design problem for optical devices. We choose to specify the performance of our device by defining the mode conversion efficiency between sets of input modes and output modes at several discrete frequencies. These modes and frequencies are specified by the user and kept fixed during the optimization process. In the limit of a continuous spectrum of frequencies, any linear optical device can be described by the coupling between sets of input and output modes, making this a remarkably general formulation[24].

Suppose the input modes $i = 1 \ldots M$ are at frequencies ω_i and can be represented by equivalent current density distributions $\mathbf{J}_i$. The electric fields $\mathbf{E}_i$ generated by the input modes should then satisfy Maxwell's equations in the frequency domain,

$$\nabla \times \mu_0^{-1} \nabla \times \mathbf{E}_i - \omega_i^2 \epsilon\, \mathbf{E}_i = -i\omega_i \mathbf{J}_i \tag{1}$$

where ϵ is the electric permittivity and μ_0 is the magnetic permeability of free space.

We can then specify N_i output modes of interest for each input mode i. We define the output mode electric fields $\mathcal{E}_{ij}$ over output surfaces S_{ij}, where $j = 1 \ldots N_i$. The device performance is then specified by constraining the amplitude coupled into each output mode to be between α_{ij} and β_{ij}. This leads to the constraint

$$\alpha_{ij} \leq \left| \iint_{S_{ij}} \mathcal{E}_{ij}^{\star} \cdot \mathbf{E}_i \mathrm{d}S \right| \leq \beta_{ij} \tag{2}$$

where we have used overlap integrals to compute the mode coupling efficiency into each output mode and assumed that the input and output modes are appropriately normalized.

The inverse design problem thus reduces to finding the permittivity ϵ and electric fields $\mathbf{E}_i$ that simultaneously satisfy the physics described by equation (1) and the device performance constraints described by equation (2). In general, we also have additional constraints on the permittivity ϵ due to fabrication limitations.

We use two methods to solve this problem, the 'objective first' method[5] and a 'steepest descent' method. In the objective first method, we constrain the electric fields $\mathbf{E}_i$ to satisfy our performance constraints in equation (2), but allow Maxwell's equations to be violated. We then minimize the violation of physics using the 'Alternating Directions Method of Multipliers' (ADMM) optimization algorithm[5]. We call this method 'objective first' because we are forcing the fields to satisfy the performance objectives first and then attempting to satisfy Maxwell's equations.

Ginzton Laboratory, Stanford University, Stanford, California 94305, USA. *e-mail: jela@stanford.edu

© 2015 Macmillan Publishers Limited. All rights reserved

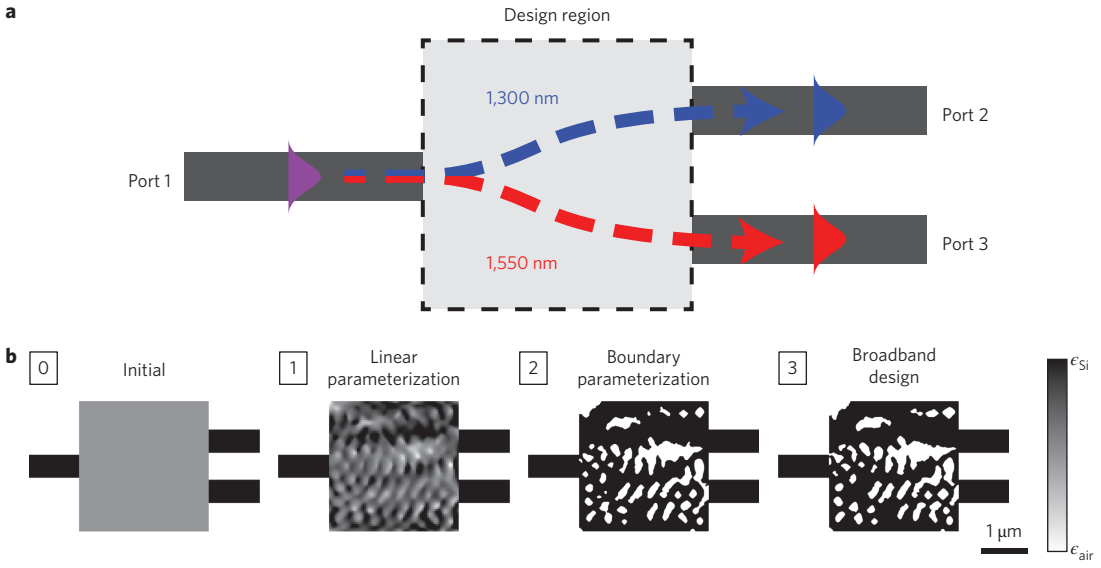


Figure 1 | Overview of the inverse design process. a, The device functionality is defined for the inverse design algorithm by specifying the surrounding structure, the design region and the coupling between a set of input and output modes. For the compact wavelength demultiplexer demonstrated in this work, the structure consists of one input waveguide, two output waveguides and a $2.8 \times 2.8\ \mu m^2$ design region. The 1,300 nm band light is coupled into the fundamental TE mode of port 2, and 1,550 nm band light is coupled into the fundamental TE mode of port 3. All three waveguides are identical, with a width of 500 nm. **b**, Intermediate structures generated by the inverse design process. In the first stage the structure is optimized while allowing the permittivity ϵ to vary continuously (linear parameterization). In the next stage we convert to a boundary parameterization and optimize the structure for operation at only 1,300 nm and 1,550 nm. In the final stage, broadband optimization is performed to generate a robust device.

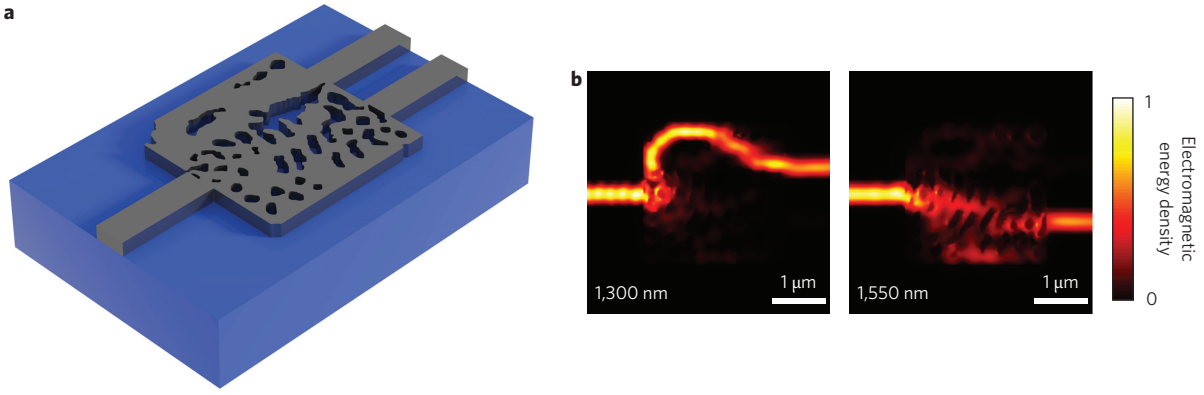


Figure 2 | The compact wavelength demultiplexer designed by the inverse design algorithm. a, A three-dimensional rendering of the structure. Silicon is shown in grey and SiO_2 in blue. Light enters the device from the input waveguide on the left-hand side and exits via one of the two output waveguides on the right. **b**, Field plots of the device operating at 1,300 nm (left) and 1,550 nm (right), calculated finite-difference time domain (FDTD) simulations. Here, we have plotted the electromagnetic energy density $U = \epsilon|\mathbf{E}|^2 + \mu|\mathbf{H}|^2$. An animated version of Fig. 2b is available in Supplementary Movie 1.

In the steepest descent method we constrain our electric fields $\mathbf{E}_i$ to satisfy Maxwell's equations and define a performance metric function based on the violation of our device performance constraints in equation (2). We then compute the local gradient of the performance metric by solving an adjoint electromagnetic problem and perform steepest-gradient descent optimization[5,14].

In designing the compact wavelength demultiplexer we chose a simple planar three-port structure with one input waveguide, two output waveguides and a square design region (Fig. 1a). For ease of fabrication, the structure was constrained to a single fully etched 220-nm-thick Si layer on a SiO_2 substrate with air cladding. Refractive indices of $n_{Si} = 3.49$, $n_{SiO_2} = 1.45$ and $n_{air} = 1$ were used. The fundamental transverse electric (TE) mode of the input waveguide was used as the input mode for the inverse design procedure, and the fundamental TE modes of the two output waveguides were used as the output modes. At 1,300 nm, we specified that >90% of the input power should be coupled out of port 2 and <1% of the power should be coupled out of port 3; the converse was specified for 1,550 nm.

The optimization processes proceeded in several stages, as outlined in Fig. 1b. In the first stage, the permittivity ϵ in the design region was allowed to vary continuously between the permittivities of silicon and air (linear parameterization). The objective first method was used to generate an initial guess for the structure, and the steepest descent method was then used to fine-tune the structure. In the second stage, the structure was converted to a binary level-set representation[25] and then optimized using steepest descent. Up to this point, the device performance had only been specified at the two centre wavelengths of 1,300 nm and 1,550 nm. In the final stage, the device was optimized for broadband performance by specifying the device performance at ten different wavelengths, with five frequencies equally spaced about each centre frequency. Broadband performance has previously been shown to

© 2015 Macmillan Publishers Limited. All rights reserved

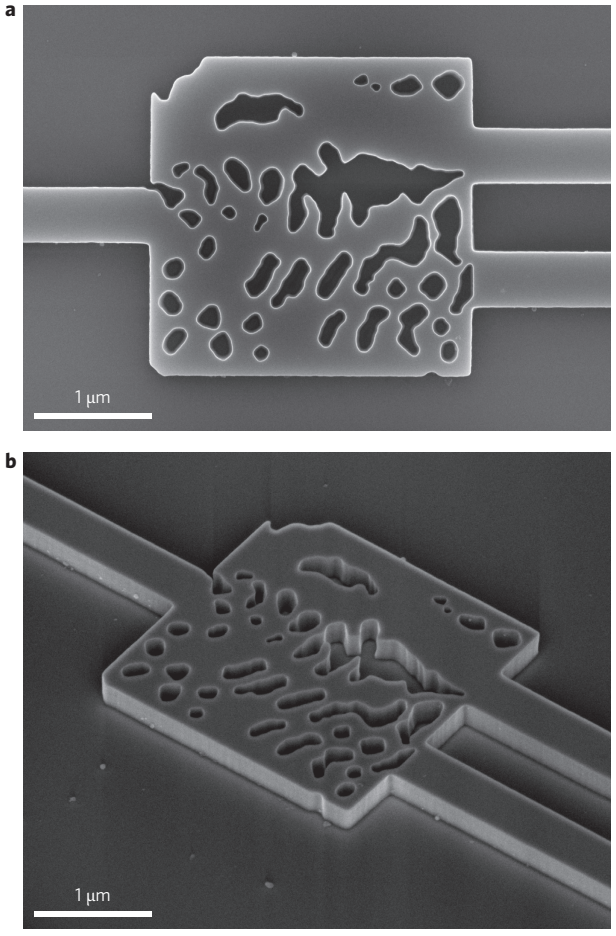


Figure 3 | SEM images of the fabricated wavelength demultiplexer. The device was fabricated by fully etching the 220-nm-thick device layer of an SOI substrate, leaving the structure with an air cladding. **a**, Top-down view. **b**, Angled view. The vertical sidewalls are clearly visible in this view.

be a heuristic for structures that are tolerant to fabrication imperfections, and it was hoped that this would result in a more robust design[5]. The WDM device was designed in ~36 h using a single server with three NVidia GTX Titan graphics cards.

The final designed device is shown in Fig. 2a. The simulated electric fields at the central operating wavelengths of 1,300 nm and 1,550 nm are plotted in Fig. 2b. At both wavelengths, the light takes a relatively confined path through the structure, despite the convoluted geometry of the etched silicon layer.

The devices were fabricated using electron-beam lithography followed by plasma etching. Scanning electron microscopy (SEM) images of a final fabricated device are shown in Fig. 3a. The original design was accurately reproduced by the fabrication process, with the exception of two small (~100 nm) holes next to the input waveguide, which are missing.

The measured and simulated scattering parameters (S-parameters) for the compact WDM device are plotted in Fig. 4. The plotted wavelength range was limited by the spectral bandwidth of the excitation source. Measurements from three identically fabricated devices are plotted together in Fig. 4b, showing that device performance is highly repeatable. Although somewhat degraded in performance with respect to the simulated devices, the fabricated WDM devices exhibit relatively low peak insertion losses of −1.8 dB and −2.4 dB in the 1,300 nm and 1,550 nm bands and broad 3 dB bandwidths of 100 nm and 170 nm, respectively. Crosstalk is less than −11 dB throughout both bands. We attribute the discrepancy between simulation and measurement to fabrication imperfections.

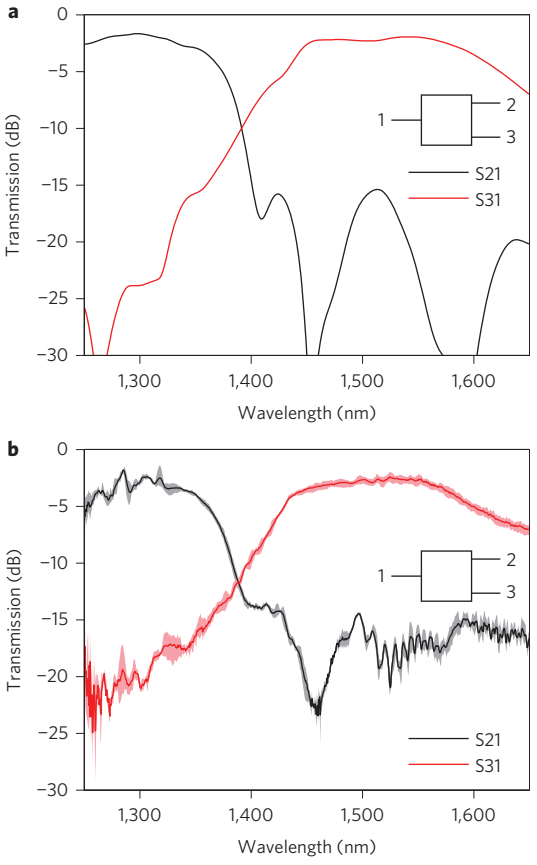


Figure 4 | S-parameters for the device, where S_{ij} is the transmission from port *j* to port *i*. a,**b**, Plots of transmission from input port 1 to output ports 2 and 3: S-parameters simulated using FDTD simulations (**a**); measured S-parameters for three identical devices (**b**). Shaded areas indicate minimum and maximum measured values across all measured devices, and solid lines indicate the average values. The measured devices exhibit relatively low peak insertion losses of -1.8 dB and -2.4 dB in the 1,300 nm and 1,550 nm bands, and broad 3 dB bandwidths of 100 nm and 170 nm, respectively. Crosstalk is less than -11 dB throughout both bands. The insertion losses and crosstalk of the device are somewhat degraded with respect to the simulated values due to fabrication imperfections.

In summary, we have experimentally demonstrated a compact, practical wavelength demultiplexer designed using our inverse design algorithm. This device provides functionality that has never before been demonstrated in such a small structure. Owing to its flexibility, our inverse design algorithm can also be applied to a wide variety of other problems and material systems, such as metamaterials and plasmonic systems. In future, the optimization algorithm could be extended to incorporate optical nonlinearities and active devices. Our results suggest that the inverse design of optical devices will revolutionize integrated photonics, ushering in a new generation of highly compact optical devices with novel functionality and high efficiencies.

Methods

Methods and any associated references are available in the online version of the paper.

Received 21 February 2015; accepted 1 April 2015;
published online 11 May 2015

References

1. Miller, D. A. B. Optical interconnects to electronic chips. *Appl. Opt.* **49,** F59–F70 (2010).

© 2015 Macmillan Publishers Limited. All rights reserved

2. Lin, V. S. Y., Motesharei, K., Dancil, K.-P. S., Sailor, M. J. & Ghadiri, M. R. A porous silicon-based optical interferometric biosensor. *Science* **278,** 840–843 (1997).
3. Kok, P. *et al.* Linear optical quantum computing with photonic qubits. *Rev. Mod. Phys.* **79,** 135–174 (2007).
4. Reed, G. T. *Silicon Photonics: The State of the Art* (Wiley, 2008).
5. Lu, J. & Vučković, J. Nanophotonic computational design. *Opt. Express* **21,** 13351–13367 (2013).
6. Ashenden, P. J. *The Designer's Guide to VHDL* 3rd edn (Morgan Kaufmann, 2008).
7. *IEEE Standard for Verilog Hardware Description Language*, IEEE Std. 1364–2001 (IEEE, 2001).
8. Jensen, J. S. & Sigmund, O. Systematic design of photonic crystal structures using topology optimization: low-loss waveguide bends. *Appl. Phys. Lett.* **84,** 2022 (2004).
9. Borel, P. I. *et al.* Topology optimization and fabrication of photonic crystal structures. *Opt. Express* **12,** 1996–2001 (2004).
10. Mutapcica, A., Boyd, S., Farjadpour, A., Johnson, S. G. & Avnielb, Y. Robust design of slow-light tapers in periodic waveguides. *Eng. Optimiz.* **41,** 365–384 (2009).
11. Jensen, J. S. & Sigmund, O. Topology optimization for nano-photonics. *Laser Photon. Rev.* **5,** 308–321 (2011).
12. Lalau-Keraly, C. M., Bhargava, S., Miller, O. D. & Yablonovitch, E. Adjoint shape optimization applied to electromagnetic design. *Opt. Express* **21,** 21693–21701 (2013).
13. Niederberger, A. C. R., Fattal, D. A., Gauger, N. R., Fan, S. & Beausoleil, R. G. Sensitivity analysis and optimization of sub-wavelength optical gratings using adjoints. *Opt. Express* **22,** 12971–12981 (2014).
14. Piggott, A. Y. *et al.* Inverse design and implementation of a wavelength demultiplexing grating coupler. *Sci. Rep.* **4,** 7210 (2014).
15. Boyd, S. & Vandenberghe, L. *Convex Optimization* (Cambridge Univ. Press, 2004).
16. Xia, F., Rooks, M., Sekaric, L. & Vlasov, Y. Ultra-compact high order ring resonator filters using submicron silicon photonic wires for on-chip optical interconnects. *Opt. Express* **15,** 11934–11941 (2007).
17. Fang, Q. *et al.* WDM multi-channel silicon photonic receiver with 320 Gbps data transmission capability. *Opt. Express* **18,** 5106–5113 (2010).
18. Alduino, A. *et al.* in *Integrated Photonics Research, Silicon and Nanophotonics and Photonics in Switching, OSA Technical Digest* PDIWI5 (Optical Society of America, 2010); http://go.nature.com/pG2HNU
19. Sasaki, K., Ohno, F., Motegi, A. & Baba, T. Arrayed waveguide grating of 70×60 μm size based on Si photonic wire waveguides. *Electron. Lett.* **41,** 801–802 (2005).
20. Horst, F., Green, W. M. J., Offrein, B. J. & Vlasov, Y. A. Silicon-on-insulator echelle grating WDM demultiplexers with two stigmatic points. *IEEE Photon. Technol. Lett.* **21,** 1743–1745 (2009).
21. Dahlem, M. S. *et al.* Reconfigurable multi-channel second-order silicon microring-resonator filterbanks for on-chip WDM systems. *Opt. Express* **19,** 306–316 (2011).
22. Bogaerts, W. *et al.* Silicon-on-insulator spectral filters fabricated with CMOS technology. *IEEE J. Quantum Electron.* **16,** 33–44 (2010).
23. Frandsen, L. H., Elesin, Y., Sigmund, O., Jensen, J. S. & Yvind, K. in *CLEO: 2013, OSA Technical Digest* CTh4 L.6 (Optical Society of America, 2013); http://go.nature.com/atKRes
24. Miller, D. A. B. All linear optical devices are mode converters. *Opt. Express* **20,** 23985–23993 (2012).
25. Osher, S. & Fedkiw, R. *Level Set Methods and Dynamic Implicit Surfaces* (Springer, 2003).

Acknowledgements

This work was supported by the Air Force Office of Scientific Research Multi-University Research Initiative (programme director G. Pomrenke; grant no. FA9550-09-1-0704). A.Y.P. acknowledges support from the Stanford Graduate Fellowship. K.G.L. acknowledges support from the Swiss National Science Foundation. J.P. was supported in part by the National Physical Science Consortium Fellowship and by stipend support from the National Security Agency. The authors thank S. Boyd for his theoretical guidance and discussions regarding the optimization algorithm. In addition, the authors thank J. Poon for the donation of the SOI wafer used to fabricate the devices.

Author contributions

A.Y.P. designed, simulated, fabricated and measured the devices. J.L. developed the inverse design algorithm and software. K.G.L. assisted in building the measurement set-up. J.P. contributed to the simulation software. T.B. provided theoretical and experimental guidance. J.V. supervised the project. All members contributed to the discussion and analysis of the results.

Additional information

Supplementary information is available in the online version of the paper. Reprints and permissions information is available online at www.nature.com/reprints. Correspondence and requests for materials should be addressed to J.V.

Competing financial interests

The authors declare no competing financial interests.

© 2015 Macmillan Publishers Limited. All rights reserved

Methods

Optimization algorithm and electromagnetic simulations. The detailed inverse design algorithm has been described elsewhere[5,14,26]. A graphical processing unit accelerated implementation of the Maxwell FDFD solver was used to efficiently solve Maxwell's equations throughout the optimization process[27,28]. An in-house graphical processing unit accelerated FDTD solver was used to run final verification simulations of the designed structure.

Fabrication. The devices were fabricated using Unibond SmartCut SOI wafers obtained from SOITEC, with a nominal 220 nm device layer and 3.0 μm buried oxide layer. A JEOL JBX-6300FS electron-beam lithography system was used to pattern a 330 nm ZEP-520A electron-beam resist layer spun on the samples. We did not compensate for the proximity effect in the electron-beam lithography step. A transformer-coupled plasma etcher was used to transfer the mask to the silicon device layer, using a C_2F_6 breakthrough step and a $BC1_3/C1_2/O_2$ chemistry main etch. The mask was stripped by soaking in Microposit Remover 1165, followed by a Piranha clean using a 4:1 ratio of concentrated sulphuric acid and 30% hydrogen peroxide. Finally, the samples were diced and polished to expose the waveguide facets for edge coupling. Detailed schematics of the device are provided in the Supplementary Section 1.

Measurements. The devices were measured by edge-coupling the input and output waveguides to lensed fibres. A polarization-maintaining (PM) lensed fibre was used on the input side to ensure that only the fundamental TE waveguide mode was excited. The polarization extinction ratio of the light emitted by the PM lensed fibre was measured using a polarizing beamsplitter to be 19.0 dB at 1,470 nm and 20.7 dB at 1,570 nm. A non-PM lensed fibre was used to collect light from the outputs. The lensed fibres were aligned by optimizing the transmission of a laser at 1,470 nm, ensuring consistent coupling regardless of the transmission characteristics of the devices.

A fibre-coupled broadband light-emitting diode source and fibre-coupled optical spectrum analyser were used to characterize the devices. The transmission measured through each device was normalized with respect to a straight-through waveguide running parallel to each device. This eliminated any coupling and waveguide losses, and yielded a direct measurement of the device efficiencies.

References

26. Lu, J. *Nanophotonic Computational Design PhD thesis, Stanford Univ*. (2013), available at http://web.stanford.edu/group/nqp/jv_files/thesis/Jesse-thesis.pdf.
27. Shin, W. & Fan, S. Choice of the perfectly matched layer boundary condition for frequency-domain Maxwell's equations solvers. *J. Comput. Phys.* **231,** 3406–3431 (2012).
28. Shin, W. MaxwellFDFD webpage (2014), available at http://web.stanford.edu/~wsshin/maxwellfdfd.html.

© 2015 Macmillan Publishers Limited. All rights reserved